Journal of Alloys and Compounds 514 (2012) 45–53

Contents lists available at SciVerse ScienceDirect

Journal of Alloys and Compounds

journal homepage: www.elsevier.com/locate/jallcom

Synthesis, magnetic and electrical characteristics of poly(2-thiophen-3-yl-malonic acid)/Fe_3O_4 nanocomposite

M. Aydın[a], B. Ünal[b,c], B. Esat[d,*], A. Baykal[c,d], E. Karaoğlu[d], M.S. Toprak[e], H. Sözeri[f]

[a] Department of Chemistry, Gebze Institute of Technology, 41400 Gebze, Kocaeli, Turkey
[b] Department of Electrical and Electronics Engineering, Fatih University, 34500, Buyukcekmece, Istanbul, Turkey
[c] BioNanoTechnology R&D Center, Fatih University, 34500 Buyukcekmece, Istanbul, Turkey
[d] Department of Chemistry, Fatih University, 34500 Buyukcekmece, Istanbul, Turkey
[e] Functional Materials Division, Royal Institute of Technology – KTH, SE16440 Stockholm, Sweden
[f] TUBITAK-UME, National Metrology Institute, PO Box 54, 41470 Gebze, Kocaeli, Turkey

ARTICLE INFO

Article history:
Received 8 June 2011
Received in revised form 18 October 2011
Accepted 19 October 2011
Available online 7 November 2011

Keywords:
Magnetic nanomaterials
Nanocomposites
Polythiophene
Conductivity
Dielectric properties

ABSTRACT

Poly(2-thiophen-3-yl-malonic acid)/Fe_3O_4 nanocomposite was synthesized by the precipitation of Fe_3O_4 in the presence of poly(2-thiophen-3-yl-malonic acid) (PT3MA). Characterizations of the nanocomposite were performed by XRD, FT-IR, TEM, TGA, AC/DC conductivity and dielectric measurements. The capping of PT3MA around Fe_3O_4 nanoparticles was confirmed by FTIR spectroscopy, the interaction being between bridging oxygen of the carboxylate and the nanoparticle surface through bidentate binding. The crystallite particle sizes of 6 ± 3 nm and 7 ± 3 nm were obtained from XRD line profile fitting and from TEM image analysis respectively, and they are in good agreement with each other. Magnetization measurements revealed that PT3MA coated magnetite particles do not saturate at higher fields. The material showed superparamagnetic character as revealed by the absence of coercivity and remnant magnetization. Magnetic particle size was calculated as 7.3 ± 1.0 nm from the mean magnetization term in the Langevin function which is also in conformity with the values determined from TEM micrographs and XRD line profile fitting. The TEM particle size analysis of the nanoparticles revealed the presence of a slightly modified magnetically dead nanoparticle surface. AC and DC conductivity measurements were performed to elucidate the electrical conduction characteristics of the product.

1. Introduction

Nanoparticulate transition-metal oxides can exhibit enhanced optical, magnetic and electrical properties when compared to their bulk counterparts, rendering nanoparticles interesting for a variety of applications [1–5]. Among these, magnetite (Fe_3O_4) is a common magnetic iron oxide that has a cubic inverse spinel structure with fcc close packed oxygen anions and Fe cations occupying interstitial tetrahedral and octahedral sites [6]. Magnetite unit cell can be represented with the formula $(Fe_8{}^{3+})_A[Fe_{40/3}{}^{3+}Fe_{8/3}{}^{2+}]_BO_{32}$, where A and B indicates tetrahedral and octahedral positioning, respectively. The rapid electron hopping between Fe^{2+} and Fe^{3+} ions in the octahedral sites at room temperature which is responsible for the good room temperature conductivity makes magnetite an important class of half-metallic materials (which are metallic in one spin direction and insulating in the other) [7]. Due to its strong magnetic and semiconducting properties, magnetite (Fe_3O_4) is one of the most preferred and well known filler materials to be used in magnetic recording media and in medical applications when combined with polymers. In addition to its magnetic properties, magnetite is unique for its very high saturation magnetization (92–100 emu/g) and an unusually low bulk resistivity ($1.068 \times 10^{-2}\ \Omega\,cm^{-1}$) [8]. Therefore, magnetite has the potential for providing the desired magnetic and electrical properties in composite materials.

Conducting polymers have attracted considerable attention for their potential applications in various fields because of their curious electronic, magnetic, and optical properties. Among them, polythiophene derivatives are particularly important, since much progress has been made in the past two decades to solve the serious problems regarding their low solubility and processability [9,10]. Their unique physical and chemical properties have made them considerably attractive materials for potential applications in the fields of drug delivery systems [11], electromagnetic interface (EMI) shielding, rechargeable batteries, electrodes and sensors, plastic transistors, and microwave absorption [12–14]. Bertran et al. [9] suggested that poly(2-thiophen-3-yl-malonic acid) is a candidate for potential applications such as selective membrane for electrodialysis, wastewater treatment, or ion-selective membrane for biomedical uses.

---

[*] Corresponding author. Tel.: +90 212 866 33 00/2065; fax: +90 212 866 34 02.
E-mail address: besat@fatih.edu.tr (B. Esat).

0925-8388/$ – see front matter © 2011 Elsevier B.V. All rights reserved.
doi:10.1016/j.jallcom.2011.10.063

Significant scientific and technological interest has focused on polymer–inorganic nanocomposites (PINCs) over the last two decades. The incorporation of inorganic nanoparticles into the polymer matrix can provide high-performance novel materials that can find applications in many industrial fields [15–19].

To the best of our knowledge, no work has been done so far on the preparation, magnetic and electrical transport properties (electronic/dielectric) of PT3MA–Fe_3O_4 nanocomposites. In the present study, we employed a simple one-pot in situ polymerization method to synthesize PT3MA–Fe_3O_4 nanocomposite and studied its structural and physical properties in detail for the first time.

2. Experimental

2.1. Materials

2-Thiophen-3-yl-malonic acid (T3MA), anhydrous iron (III) chloride (98%) ($FeCl_3$), ammonium hydroxide (NH_4OH), iron (III) nitrate nonahydrate ($Fe(NO_3)_3{\cdot}9H_2O$, 98%) iron (II) chloride tetrahydrate ($FeCl_2{\cdot}4H_2O$, 98%), concentrated sulfuric acid (H_2SO_4), hydrochloric acid (HCl), sodium hydroxide (NaOH) were all of analytical purity (obtained from Merck and Sigma–Aldrich) and used as-received, without any purification.

2.2. Characterization techniques

X-ray powder diffraction (XRD) analysis was conducted on a Rigaku Smart Lab operated at 40 kV and 35 mA using Cu K_α radiation (λ = 1.54059 Å).

Fourier transform infrared (FT-IR) spectra of the samples were recorded with a Perkin Elmer BX FT-IR infrared spectrometer equipped with an diamond attenuated total reflectance (ATR) accessory in the range of 4000–400 cm^{-1} with better than 4 cm^{-1} resolution.

Transmission electron microscopy (TEM) analysis was performed using a JEOL/JEM 2100 microscope. A drop of diluted sample in alcohol was dripped on a TEM grid.

The thermal stability was determined by thermogravimetric analysis (TGA, Perkin Elmer Instruments model, STA 6000). The TGA thermograms were recorded for 5 mg of powder sample at a heating rate of 10 °C/min in the temperature range of 30–800 °C under nitrogen atmosphere.

The electrical conductivities of the PT3MA and PT3MA/Fe_3O_4 nanocomposite were studied in the range of 20–150 °C with 10 °C steps. The samples used were in the form of circular pellets with a diameter of 13 mm and thickness of 3 mm. The pellets were sandwiched between gold electrodes and the conductivities were measured using Novocontrol dielectric impedance analyzer in the frequency range 1 Hz–3 MHz. The temperature was controlled with a Novocool Cryosystem, between −100 °C and 250 °C. The dielectric data (ε' and ε'') were collected during heating as a function of frequency.

VSM measurements were performed using a vibrating sample magnetometer (LDJ Electronics Inc., Model 9600). The magnetization measurements were carried out in an external field up to 15 kOe at room temperature.

The NMR spectra were taken in the suitable solvents using Bruker Avence III 400 MHz NMR Spectrometer.

Gel permeation chromatography (GPC) measurements were performed on tetrahydrofuran (THF) solutions of the polymers (only on the THF soluble portions of each polymer) using a GPC 1100 (Agilent) instrument. The measurements were standardized against THF solutions of a polystyrene standard.

UV-visible (UV–vis) measurements were carried out with a Unicam double-beam spectrophotometer. Stock solutions of the monomers and polymers were prepared by dissolving a few milligrams of the solid in 1–2 ml $CHCl_3$. These stock solutions were diluted if necessary.

2.3. Synthesis of PT3MA

PT3MA and its monomer (T3MA) were successfully synthesized and characterized as described in Supplementary section.

2.4. Synthesis of PT3MA/Fe_3O_4 nanocomposite

Stoichiometric amounts of Fe(III) and Fe(II) chloride salts (with a molar ratio of 2:1) and 50 mg of PT3MA were dissolved in 100 ml distilled water under vigorous stirring. Then a 2 M aqueous NaOH solution was added very slowly until the pH was raised to ~11 and a black suspension was formed. This suspension was then refluxed at 90 °C for 12 h, under vigorous stirring and Ar gas. Magnetic particles were separated from the aqueous solution by magnetic decantation, washed with distilled water several times and then dried in an oven overnight.

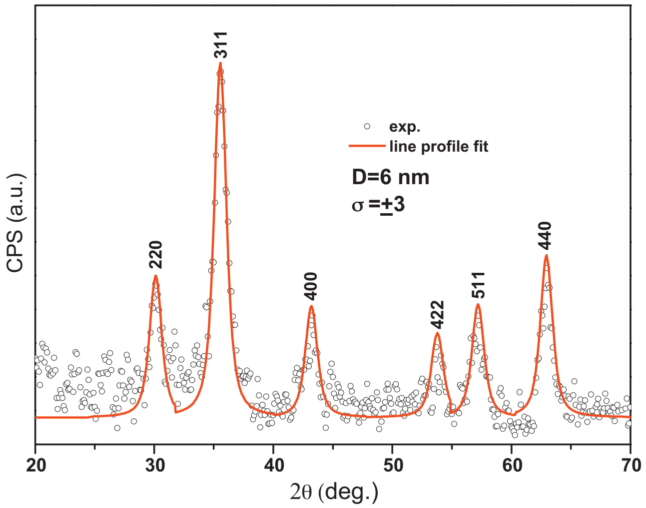

Fig. 1. XRD pattern and line profile fitting of PT3MA–Fe_3O_4 nanocomposite.

3. Results and discussion

3.1. XRD analysis

Phase investigation of the crystalline product was performed by XRD and the diffraction pattern is presented in Fig. 1. The XRD pattern indicates that the product consists of magnetite, Fe_3O_4, and the diffraction peaks are broadened owing to very small crystallite size. All of the observed diffraction peaks are indexed by the cubic structure of Fe_3O_4 (JCPDS no. 19-629) revealing a high phase purity of magnetite. The mean size of the crystallites was estimated from the diffraction pattern by line profile fitting method using Eq. (1) following the method given in Refs. [11,12]. The line profile, shown in Fig. 1 was fitted for observed six peaks with the following miller indices: (2 2 0), (3 1 1), (4 0 0), (4 2 2), (5 1 1), (4 4 0). The average crystallite size, D, was obtained as 6 ± 3 nm as a result of this line profile fitting.

3.2. FT-IR analysis

FT-IR spectra of PT3MA–Fe_3O_4 nanocomposite and PT3MA, were given Fig. 2b and c respectively. In the spectrum of PT3MA coated Fe_3O_4 (Fig. 2b), the asymmetric and symmetric CH_2 stretching vibrations shifted to 2922 and 2852 cm^{-1}, respectively. The position of the asymmetric carboxylate stretching vibration decreased to 1620 cm^{-1} and got broader in FTIR spectrum of P3TMA as compared to that of the monomer (FTIR spectrum of T3MA is presented in Supplementary section) due to increased amount of hydrogen bonding interactions. In addition, the O–H stretching vibration (observed between 3600 and 1750 cm^{-1}) is much broader in PT3MA compared to that of the monomer. In Fig. 2c, asymmetric and symmetric stretching frequencies of carboxylate (COO^-) of PT3MA are observed at 1620 cm^{-1} and 1403 cm^{-1} respectively. In the spectrum for PT3MA–Fe_3O_4 nanocomposite (Fig. 2b), the vibrations of asymmetric and symmetric stretching of carboxylate anion occurred at 1621 and 1340 cm^{-1}. The splitting between asymmetric and symmetric stretching of carboxyl group, $\Delta\nu$ ($\nu_{\mathrm{asymmOCO}} - \nu_{\mathrm{symOCO}}$), is higher than that present in the FT-IR spectra of uncoordinated PT3MA (Fig. 2c), indicating a bidentate coordination between the carboxyl anions and the metal ions [20,21] as schematically depicted in Fig. 2a.

The inorganic lattice vibration appears in the range 400–700 cm^{-1} (Fig. 2b). The FTIR of the prepared powder shows characteristic peaks that are exhibited by the commercial magnetite powder: The metal–oxygen band, ν_1, observed at 590 cm^{-1}

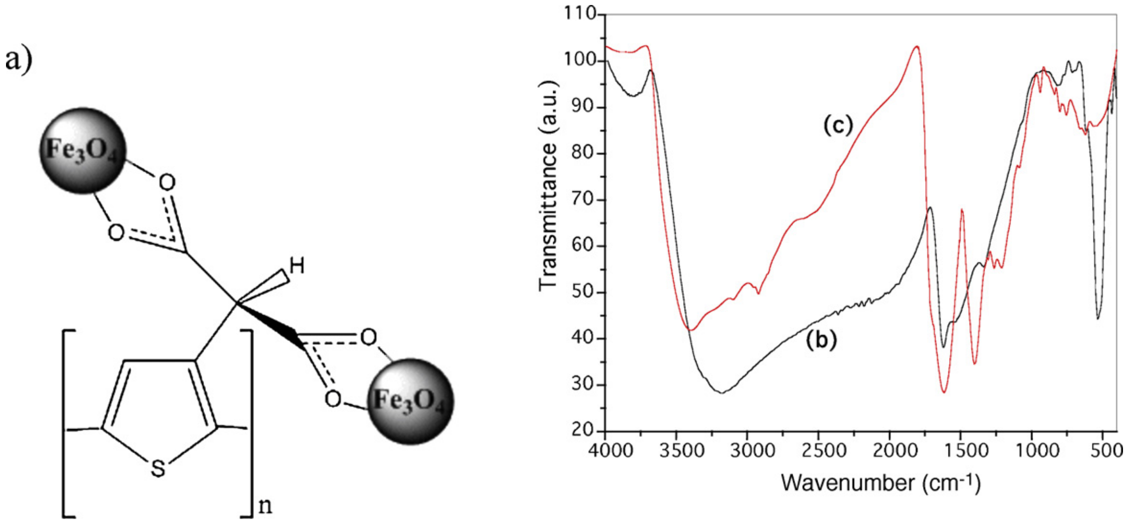

Fig. 2. (a) Suggested linkage of PT3MA to iron oxide surface FT-IR spectra of (b) PT3MA–Fe_3O_4 nanocomposite and (c) PT3MA.

corresponds to intrinsic stretching vibrations of the metal at tetrahedral site ($Fe_{\text{tetra}} \leftrightarrow O$), whereas the metal–oxygen band observed at 445 cm^{-1}, υ_2, is assigned to octahedral-metal stretching ($Fe_{\text{octa}} \leftrightarrow O$) [22–27].

3.3. TEM analysis

TEM micrographs of PT3MA/Fe_3O_4 nanocomposite are shown in Fig. 3a and b. The size distribution diagram is presented in Fig. 3c. The particles were observed to have a spherical morphology. Size distribution histogram was obtained by measuring at least 150 nanoparticles and it was fitted using a log-normal function [28]. An average size, $D_{\text{TEM/log-normal}}$, of ~6 nm was obtained for magnetite nanoparticles. Crystallite size obtained from XRD line profile fitting was very similar to the particle size estimated from TEM, revealing nearly single crystalline nature of the nanoparticles. High resolution TEM image presented in Fig. 3b reveals atomic planes and the distance measured can be assigned to (2 2 0) plane for magnetite corresponding to a distance of ~3 Å. In this image, a very thin layer of polymer (PT3MA) coating around the particles can also be observed.

3.4. TG analysis

TGA thermograms of nanocomposite and PT3MA are presented in Fig. 4, which can be used for a quantitative comparison of degradation behavior of both the polymer and the nanocomposite samples. Iron oxide showed no weight loss in the temperature range of TG analysis [29–32]. On the other hand, a degradation was clearly seen in the TGA curves of the nanocomposite. Combustion of PT3MA was not complete within the temperature interval of the analysis. Approximately 85% of the polymer was decomposed at 750 °C. However, nanocomposite showed only a slight weight loss of about 12% at this temperature. Based on the thermogram and the above discussions, PT3MA amount in the composite was predicted to be around 10–15%, which indicated an inorganic content of about 85–90%.

3.5. VSM analysis

The room temperature magnetization curve of PT3MA coated magnetite was measured up to 15 kOe using a vibrating sample magnetometer, see Fig. 5. The specific saturation magnetizations (M_s) of the composite and bulk magnetite were calculated from a plot of M versus $1/H$ (M at $1/H \geq 0$) as 49 and 55 emu/g (normalized to the mass of the magnetic core), respectively. M_s of bulk magnetite was considerably lower compared to its theoretically determined value of 92 emu/g. Fig. 5 also revealed that magnetizations of bulk and coated magnetites could not reach to saturation. The samples showed no coercivity and hysteresis behavior. All of these observations are characteristic features of superparamagnetic (SP) particles having grain sizes less than 20 nm [33]. Reduced magnetization is generally observed in SP magnetite particles and can be explained by spin canting and presence of disordered spins at the surface [29,31,34–37]. The effect of surface spins on overall magnetization increases due to the presence of a considerably increasing fraction of spins on the surface as particle size decreases. In addition to spin canting and disordered spins, adsorption of surfactant molecules onto the surface of magnetite can also decrease the magnetization. As also observed in our previous works [29,32,38], the polymeric surfactant molecules are bound to the magnetite surface over oxygen atoms (see Section 3.2). Therefore, some of the spins of the oxygen atoms close to the surface are pinned and this weakens the super exchange interaction between Fe–O–Fe atoms, causing the overall magnetization of the nanocomposite to decrease.

Magnetization of superparamagnetic particles is described by the Langevin function (Eq. (1)) which can also be used to determine the particle size;

$$M = M_s \left\{ \coth\left(\frac{\mu H}{k_B T}\right) - \frac{k_B T}{\mu H} \right\} \quad (1)$$

here μ denotes the mean magnetic moment of a single particle, H is the applied field and $k_B T$ term corresponds to the thermal energy of the particles. The Langevin relation considers each particle as a magnetic monodomain. The relationship between the mean magnetic moment of a particle and saturation magnetization of particles, as described by Eq. (2), can be used to calculate average particle size, D;

$$\mu = \frac{M_s \pi \rho D^3}{6} \quad (2)$$

where ρ is the density of the sample.

Mean magnetic moment (μ) was determined as 5046μ_B at 300 K by fitting Eq. (1) to M–H hysteresis curve of the composite. Then, by substituting this value in Eq. (2), mean particle size was calculated to be 7.3 ± 1.0 nm, which agrees well with the values calculated from XRD patterns (6.0 ± 3.0 nm).

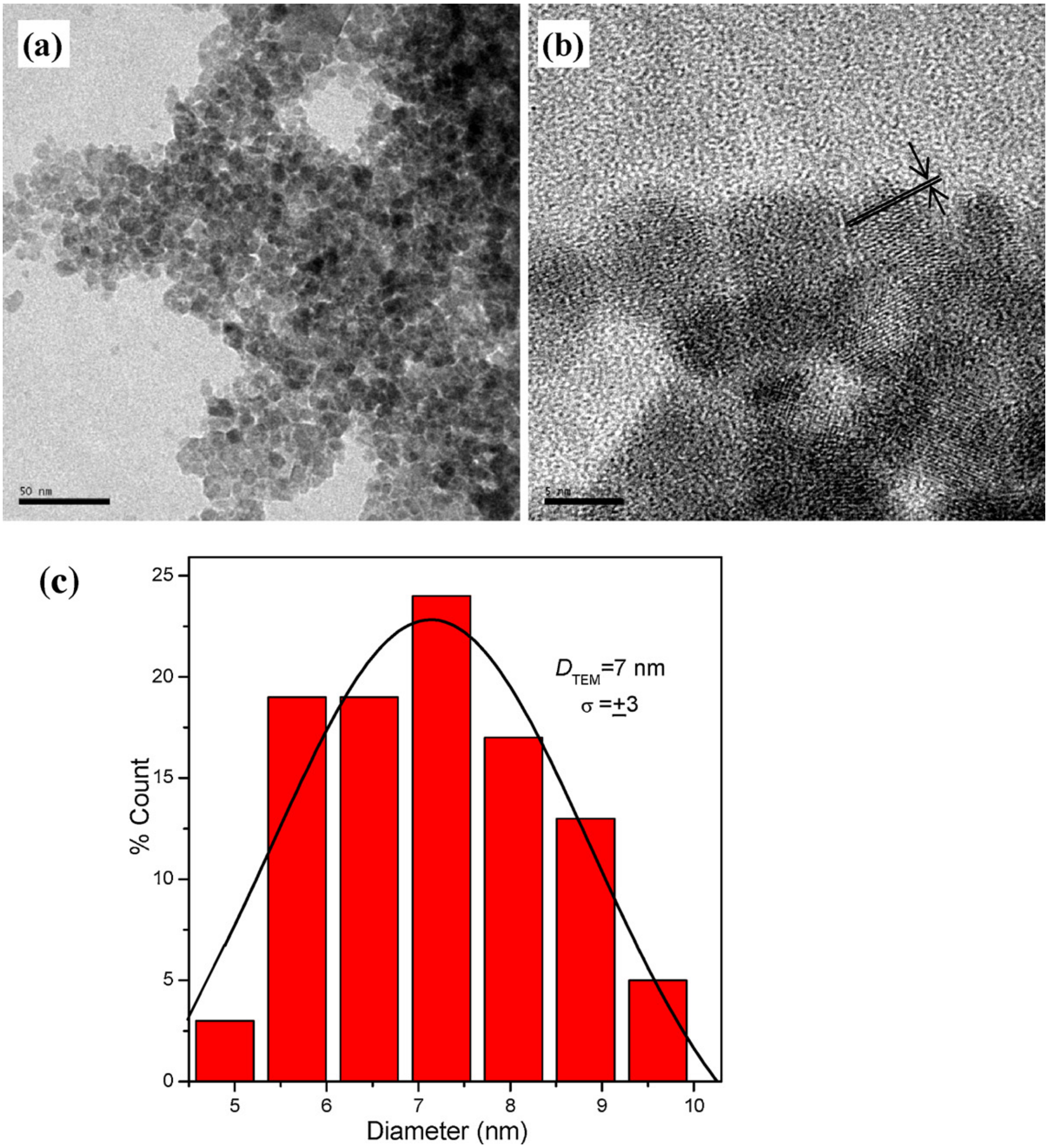

Fig. 3. (a and b) TEM micrographs of PT3MA–Fe_3O_4 nanocomposite at different magnifications; (c) size distribution histogram obtained from TEM micrographs.

3.6. Conductivity measurements

For any conductive nanocomposite material, it is very important to understand how the conductivity changes with temperature for the different temperature ranges concerned. The inherent conductivities can be assumed, in general, to be more or less equal. However, the physical characteristics like density and orientation of the polymeric particles are significantly varied depending on the material content in nanocomposites. Because of low density and random orientation of most polymeric nanoparticles, the contact among the particles throughout the crystallite boundaries is poor and this may results in a relatively low conductivity in the nanocomposite materials [31,32]. At lower temperatures, magnetite nanoparticles surrounded by PT3MA initially form a random network. When temperature is increased steadily, nanocomposites of magnetites enclosed by PT3MA starts to become more organized into a matrix form in which each capped network in the matrix shows both capacitive and resistive behaviors. The amount of equivalent components in the material is dependent on the range of the transition temperature as modeled in the literature [31,32]. This phenomenon can be entitled as a formation of the temperature-assisted nanolattices of capped magnetite nanoparticles. This results in the change of overall conductivity with temperature because of the temperature-assisted reorganization among magnetites and PT3MA.

The ac conductivities, σ_{ac} (ω) of both the PT3MA polymer nanoparticles and PT3MA–Fe_3O_4 nanocomposite studied here were measured between 20 °C and 150 °C using impedance spectroscopy and results were shown in Figs. 6–9. Frequency-dependent ac conductivity, σ_{ac} (ω), was obtained using Eq. (3);

$$\sigma'(\omega) = \sigma_{ac}(\omega) = \in''(\omega)\omega\varepsilon_0 \tag{3}$$

where σ' (ω) is the real part of conductivity, ω is the angular frequency of the signal applied across the sample, $\in''$ is the

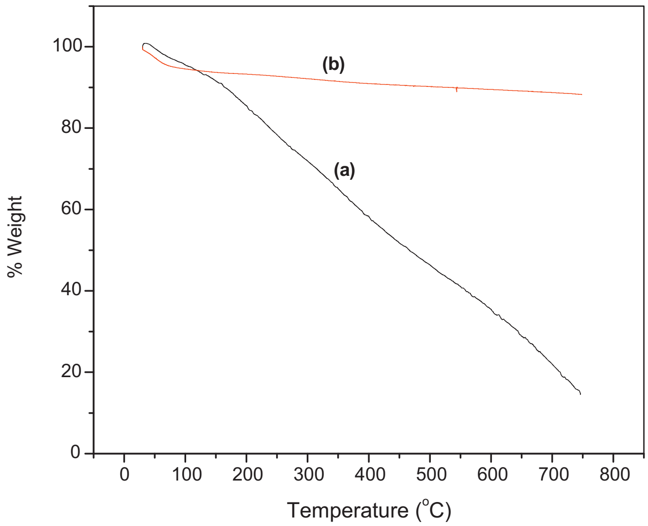

Fig. 4. TGA thermograms of (a) PT3MA and (b) PT3MA–Fe_3O_4 nanocomposite.

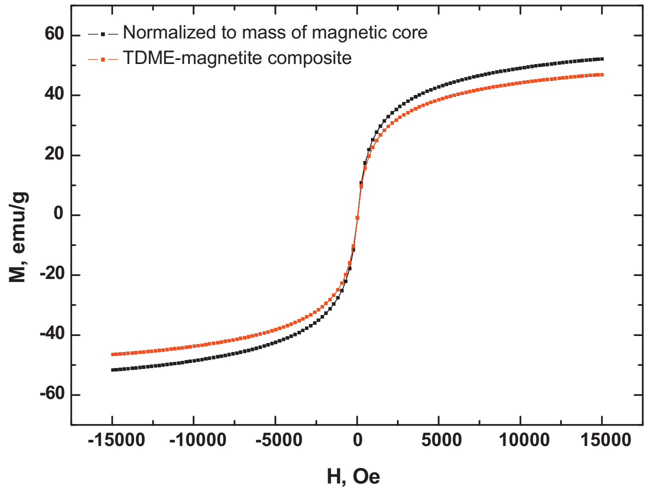

Fig. 5. Room temperature *M–H* curve for PT3MA–Fe_3O_4 nanocomposite.

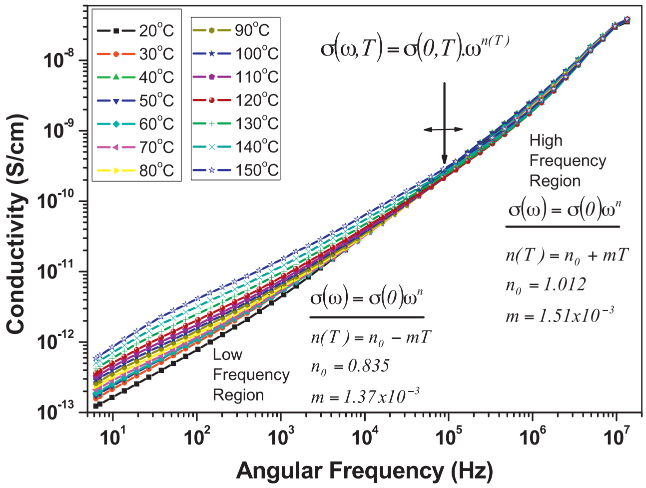

Fig. 6. AC conductivity of PT3MA polymer nanoparticles versus angular frequency for temperatures ranging from 20 to 150 °C.

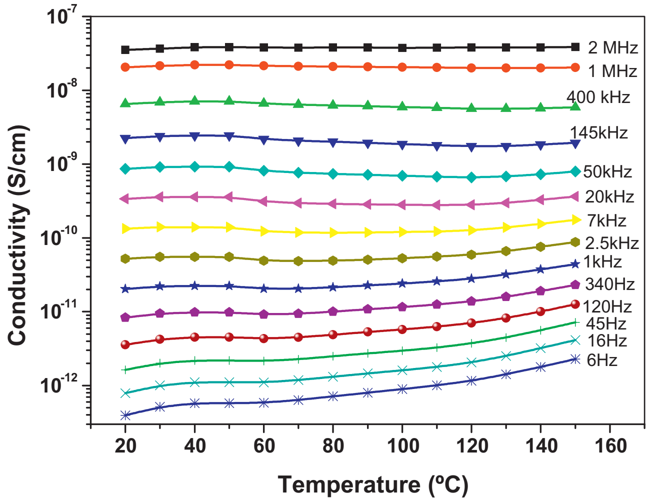

Fig. 7. AC conductivity plotted against temperatures for a PT3MA polymer nanocomposite at frequencies ranging from 6 Hz to 2 MHz.

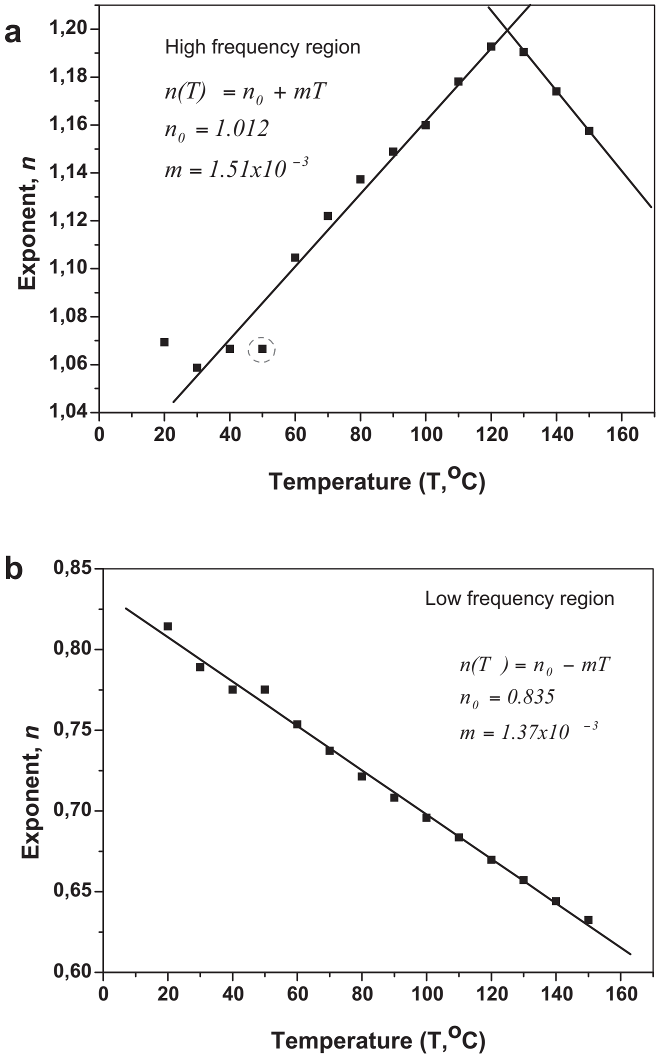

Fig. 8. Variation of frequency-dependent power exponent as a function of temperature (a) at frequency (b) low frequency regions $\sigma(\omega, T) = \sigma(0, T) \cdot \omega^{n(T)}$.

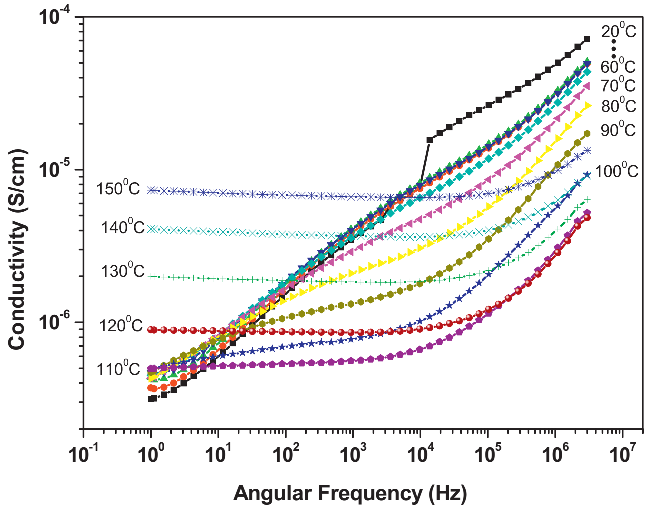

Fig. 9. AC conductivity versus angular frequency dependence for PT3MA–Fe_3O_4 nanocomposite from RT to 150 °C.

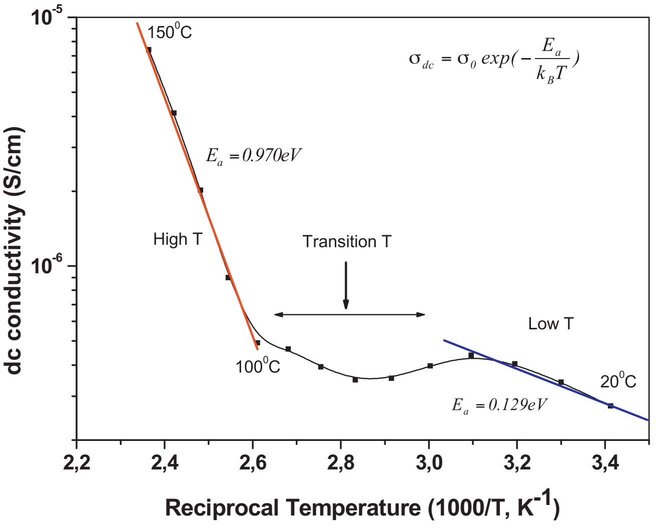

Fig. 10. DC conductivity of PT3MA–Fe_3O_4 nanocomposite as a function of reciprocal temperature.

imaginary part of complex dielectric permittivity (ϵ^*) and ε_0 (8.852×10^{-14} F/cm) is the vacuum permittivity.

As can be seen from the ac conductivity behavior of PT3MA polymer nanoparticles (Fig. 6), the conductivity was found to be temperature dependent in low frequency region, while it was observed to be less frequency-dependent in high frequency region. This shows that the capacitive effect is more prevailing. The ac conductivity of PT3MA polymer nanoparticles was found to obey an exponential function of angular frequency formulated as $\sigma(\omega, T) = \sigma(0, T) \cdot \omega^{n(T)}$ where each power exponent, $n(T)$, is temperature-dependent in a different manner in both the low and high frequency regions. Variation of frequency-dependent power exponent as a function of temperature in regions of both higher and lower frequencies is represented in Fig. 8 where the power exponents of ac conductivity comply with linear fits having both positive and negative slopes, respectively. This can be attributed to the variation of ac conductivity profiles with temperature and frequency, which may be caused by both structural changes due to the effect of temperature and electrical influence of frequency on conductivity.

In Fig. 7, conductivities taken at various frequencies were plotted as a function of temperature. Here at lower frequencies, the conductivity increased almost exponentially with temperature as expected. Nevertheless, at higher frequencies, it remained almost unchanged. This can be attributed to the capacitive effects at higher frequencies among the nanoparticles. Additionally, electron hopping process may have a difficulty to follow the externally applied ac electric field.

As can be seen from Fig. 9, the curves of ac conductivity versus angular frequency at various temperatures comprise conductivity plateau regions in general, while the plateau region for hot nanocomposite is well developed at low frequencies. The plateau region at lower temperatures was slightly less distinguishable at medium frequencies, and shifted toward higher frequencies with increasing temperature, especially over 70 °C. In other words, the conductivity plateau regions, which were well developed at lower frequencies and above 70 °C, broadened toward higher frequencies at higher temperatures. The conductivity seemed to follow the function $\sigma(\omega, T) = \sigma(0, T) \cdot \omega^{n(T)}$. At temperatures above 100 °C, the structural reorganization seemed to be settled down and ac conductivity at lower frequency became less frequency-dependent.

The variation of dc conductivity of the PT3MA–Fe_3O_4 nanocomposite with T was demonstrated in Fig. 10. The conductivity curve demonstrated that dc conductivity depended strongly on temperature (in the regions of linear fittings of the conductivity versus $1/T$ curve).

Generally, PT3MA-capped systems exhibited Arrhenius behavior at various temperature ranges below and above a transition region which has a width of 60 °C about 130 °C. The conductivity isotherm at low and high temperature can be fitted with Arrhenius equation as follows [39];

$$\sigma_{\mathrm{dc}} = \sigma_0 \quad \exp\left(-\frac{E_0}{k_{\mathrm{B}} T}\right)$$

where σ_0 is the pre-exponential terms, E_{a} is the activation energy for each region and k_{B} (8.617385×10^{-5} eV/K) is the Boltzmann constant. Two different activation energies of $E_{\mathrm{a}} = 0.129$ eV and 0.970 eV were obtained in temperature ranges below and above the transition range temperatures, respectively. It was clearly seen that electrical conductivity was strongly dependent on temperature. So, dc conductivity of the PT3MA capped magnetite nanocomposites can be classified into three regions over a limited temperature range from RT to 150 °C. While transition region observed between temperatures 45 °C and 95 °C showed a metallic-like behavior, which means electrical conductivity decreases with increasing temperature. Dc electrical conductivity increases with increased temperature with the formulation of $\log \sigma_{\mathrm{dc}}$ versus $1/T$ before and after this transition region as shown in Fig. 10. Accordingly, this semiconducting phase obeys Mott's variable range hopping mechanism of the conduction because the conduction mechanism of the nanocomposite shows a crossover from the Mott's law, $\exp(-AT^{-1/4})$ [39,40], to a simply activated law, $\exp(-(\Delta E/k_{\mathrm{B}}T))$. This dependence can be often conveyed as a slope in logarithmic conductivity versus reciprocal temperature graphs. So, this behavior can be attributed to the temperature-induced transition from three dimensional hopping conduction in a network of weakly interconnected nanoparticles to thermally activated behavior [41,42], where the physical meaning of the one fourth exponent in Mott's law can be ascribed to the reciprocal of the effective dimensionality of four (three spatial plus one energy) [43]. Here, it should be emphasized that due to ferrites' semiconducting nature, the conductivity increases with increasing temperature.

3.7. Impedance measurements

The impedance measurements of the complex dielectric permittivity with real ε' and imaginary ε'' components of the

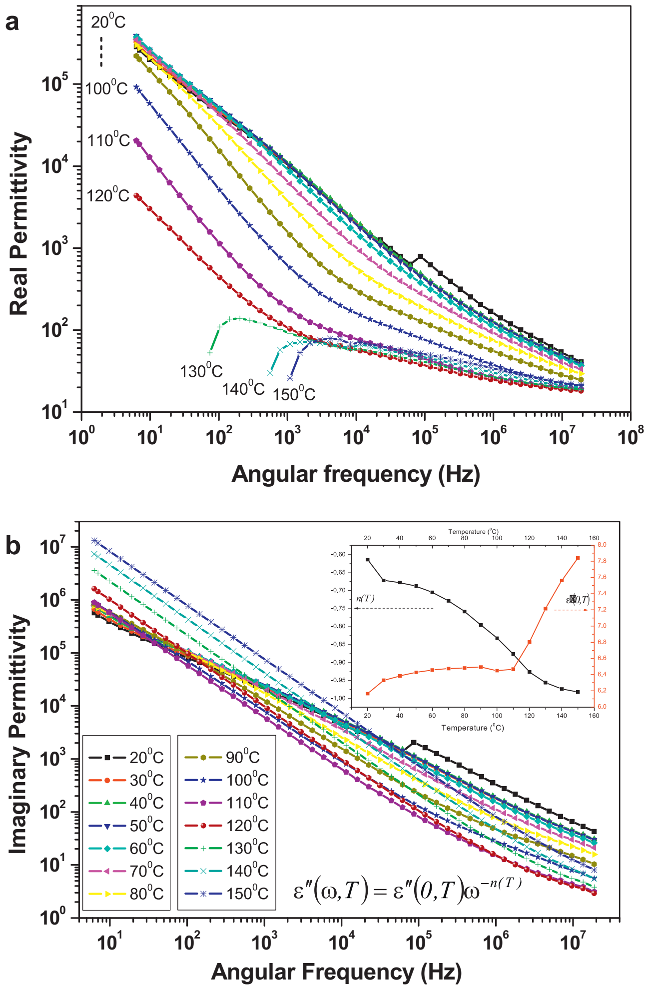

Fig. 11. (a) Real and (b) imaginary parts of permittivity of PT3MA–Fe_3O_4 nanocomposite as a function of frequency at various temperatures.

PT3MA–Fe_3O_4 nanocomposite were performed. The real component of permittivity as a function of frequency at various temperatures was shown in Fig. 11. In general, the real component of permittivity for the nanocomposite studied decreased sharply with increasing frequency in the lower frequency range at lower temperatures. While at higher temperatures, the decline in real part was very slow and also the real component's intensity was quite low. This is an expected result because of a possible structural reorganization of nanocomposite at high temperatures as a whole, and of a phase transition in the medium temperature range. At higher temperatures the variation of the real part of permittivity may be less important to some extent in applying external electric field with higher frequency. There was an interesting and unclear variation in real part of permittivity at temperatures above 130 °C. No real part was recorded at lower frequencies and its magnitude increased at first and then decreased in the log–log plot of real permittivity versus angular frequency of the applied signal. In general, real permittivity could be considered to obey $\varepsilon'(\omega, T) = \varepsilon'(0)\omega^{-n(t)}$ within some limited region of different power exponent $n(T)$ except for the initial part of higher temperature and lower frequency region as shown in Fig. 11a.

Imaginary part of dielectric permittivity versus angular frequency for temperatures ranging from RT to 150 °C was studied concisely as shown in Fig. 11b. From the fitting parameters, logarithmic imaginary part of the permittivity remained unchanged for various temperatures while the exponent “n” (between 0.6 and 1.0) was found to increase almost linearly with temperatures as shown in the inset of Fig. 11b. This attitude showed us that, on one hand, the capacitive response of the nanocomposites was less-dependent on temperature and more dependent on the nature of the reorganization of the PT3MA capped magnetite nanoparticles. On the other hand, imaginary part was found to be dependent on reciprocal of angular frequency of the applied signal as given by $\varepsilon''(\omega, T) = \varepsilon''(0)\omega^{-n(T)}$. Within the frequency range of measurements, the imaginary parts of the effective permittivity of nanocomposite exhibited spectra which can be analytically well represented by power laws. The associated power law exponents of imaginary parts of the permittivity were in the range 0.6–1.0 which was in agreement with data earlier reported [31,32,44].

Consequently, the dielectric constant increased usually with increasing temperature as seen in semiconducting materials. This can be resembled to some cases in which the thermal energy converts the bound charges into the charge carriers. This intensifying charge carrier concentration always leads to easy alignment of dipoles in the applied ac electrical field and accordingly to increases in dielectric constants. Furthermore, the mobility of the charge carriers increases with increasing temperature because of the building up of thermal energy.

Electric modulus formalism is a preferential method to study the polarization effect. So, the electric modulus can be calculated by Eq. (4) [45,46];

$$M^* = (\varepsilon^*)^{-1} = M' + iM'' = \frac{\varepsilon'}{\varepsilon'^2 + \varepsilon''^2} + i\frac{\varepsilon''}{\varepsilon'^2 + \varepsilon''^2} \tag{4}$$

Fig. 12 shows the real and imaginary part of electric modulus formalism of the PT3MA–Fe_3O_4 nanocomposite. As shown, both parts of modulus (M^*) increased with angular frequency obeying a power law that can be formulated as $M^*(\omega, T) = M^*(0)\omega^{n(T)}$ for three temperature regions (low: 20–80 °C, medium: 90–120 °C; and higher: above 120 °C). And then, they reached a constant value and became saturated at higher frequency, as expected. The starting points of the curves depend strongly on the temperature. Additionally, the entire formalism attitude of both real and imaginary parts of the electrical modulus strongly depended on the temperature over three different regional tendencies. The power law exponents can have a value dependent on the temperature regions. This type of relaxation processes might be attributed to an interfacial polarization effects.

According to the electric modulus formalism, the temperature and frequency dependencies of dielectric properties of the PT3MA–Fe_3O_4 nanocomposites can be explained as follows [47,48]. When the temperature is reduced, the expansion of PT3MA matrix will separate the filling components of the nanocomposite that were once connected with each other. The interfaces between magnetites and PT3MA matrix will enhance, and the dielectric constant will increase. When the temperature is raised higher than a certain value, the PT3MA nanocrystallite phase begins to change, transforming from a semi-crystalline phase to the polymer-like region. The interfaces between the magnetites and PT3MA matrix will remain unchanged. So, the dielectric constant will become constant. The polarization effect becomes important. As it is well known, solid polymer electrolytes have several advantages over the liquid counterpart such as desirable shape mouldability, mechanical strength and flexibility of design. Unfortunately, solid polymer electrolytes have the intuitive problem of low ionic conductivity at ambient temperatures that acts as a barrier to their suitability. It can be understood that various physical and chemical factors such as crystallinity, synchronized cation–anion motions and the formation of the ion-pairs have a strong effect on ionic conductivity [49,50]. These factors reduce the cationic conductivity, and therefore this act as a barrier for potential applications.

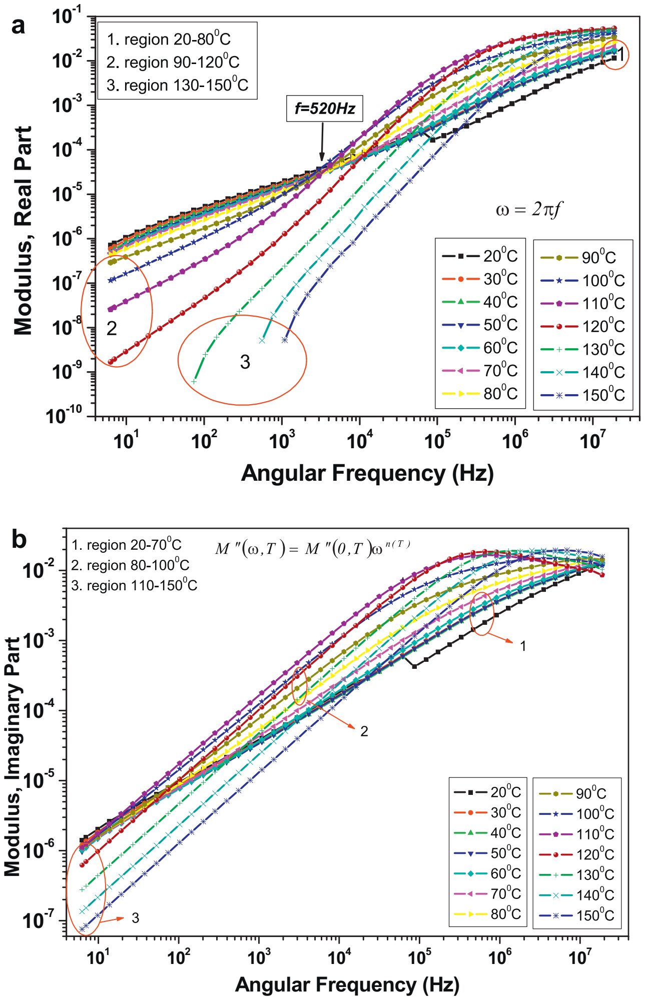

Fig. 12. (a) Real and (b) imaginary part of electric modulus of PT3MA–Fe_3O_4 nanocomposites.

As a general rule, it is well-known that there are a few different mechanisms which influence the shape of the permittivity versus frequency curves for a variety of temperature regions. First of all, there are relaxation effects which can be associated with permanent and induced molecular dipoles. At low frequencies, the applied electric field varies slowly enough to allow dipoles to reach equilibrium before the field is measurably changed. At higher frequencies, at which dipole orientations cannot track the applied field due to the viscosity of the medium, the absorption of the field energy results in energy dissipation. The mechanism of dipoles relaxing is termed as dielectric relaxation. There are also resonance effects which originate from the rotations or vibrations of atoms, ions, or electrons. These processes are examined in the neighborhood of their characteristic absorption frequencies.

4. Conclusions

In this study the preparation, magnetic and electrical transport properties (electronic/dielectric) of PT3MA–Fe_3O_4 nanocomposite were presented. The crystallite particle sizes were obtained from XRD, TEM and VSM as 6 ± 3 nm, 7 ± 3 nm and 7.3 ± 1.0 nm respectively. FT-IR study indicated a bidentate coordination between the carboxyl anions and the metal ions. AC and DC conductivity measurements revealed semiconductor conduction characteristics, and various trends were observed, as a function of frequency and temperature, revealing different mechanisms dominating based on the temperature dependant reorganization of the nanocomposite. Permittivity measurements showed increasing dielectric constant with increasing temperature as expected from semiconducting materials. Analysis of electrical modulus and dielectric permittivity functions suggested that ionic and polymer segmental motions were strongly coupled in the nanocomposite. M_s of bulk magnetite was considerably lower compared to its theoretically determined value of 92 emu/g. Magnetization of bulk and coated magnetite did not reach to saturation and showed no coercivity and hysteresis behavior.

Acknowledgements

The authors are thankful to the Fatih University, Research Project Foundation (Contract no: P50020902-2) and Scientific and Technological Research Council of Turkey (TÜBİTAK) (Project no:110T487) for financial support of this study. Authors thank Dr. O. Duygulu for his help with TEM measurements.

Appendix A. Supplementary data

Supplementary data associated with this article can be found, in the online version, at doi:10.1016/j.jallcom.2011.10.063.

References

[1] D.K. Kim, M.S. Amin, S. Elborai, S.H. Lee, Y. Köseoğlu, M. Muhammed, J. Appl. Phys. 97 (2005) 10J510.
[2] R.R. Salunkhe, K. Jang, H. Yu, S. Yu, T. Ganesh, S.-H. Han, H. Ahn, J. Alloys Compd. 509 (2011) 6677.
[3] D.T.T. Nguyet, N.P. Duong, L.T. Hung, T.D. Hien, T. Satoh, J. Alloys Compd. 509 (2011) 6621.
[4] B. Roy, S. Das, J. Alloys Compd. 509 (2011) 5537.
[5] B. Yan, F. Lei, J. Alloys Compd. 507 (2010) 460.
[6] R.M. Cornell, U. Schwertmann, The Iron Oxides: Structure, Properties, Reactions Occurrence and Uses, VCH, New York, 1996.
[7] S. Soeya, J. Hayakawa, H. Takahashi, K. Ito, C. Yamamoto, A. Kida, H. Asano, M. Matsui, Appl. Phys. Lett. 80 (2002) 823;
E.J.W. Verwey, Nature 144 (1939) 327.
[8] S.A. Liong, Multifunctional approach to development, fabrication, and characterization of Fe_3O_4 composites, Doctoral Thesis, Georgia Institute of Technology, USA, 2005.
[9] O. Bertran, E. Armelin, F. Estrany, A. Gomes, J. Torras, C. Alemán, J. Phys. Chem. B 114 (2010) 6281.
[10] M. Aydın, Z. Durmus, H. Kavas, B. Esat, H. Sozeri, A. Baykal, F. Yılmaz, M.S. Toprak, Polyhedron 30 (2011) 1120.
[11] C. Wang, Z.X. Guo, S. Fu, W. Wu, D. Zhu, Prog. Polym. Sci. 29 (2004) 1079.
[12] J.Q. Kan, X.H. Pan, C. Chen, Biosens. Bioelectron. 19 (2004) 1635.
[13] G.B. Blanchet, C.R. Fincher, F. Gao, Appl. Phys. Lett. 82 (2003) 1290.
[14] Y.-M. Bai, P. Qiu, Z.-L. Wen, S.-C. Han, J. Alloys Compd. 508 (2010) 1.
[15] S. Li, M.M. Lin, M.S. Toprak, D.K. Kim, M. Muhammed, Nano Rev. 1 (2010) 5214.
[16] Y. Li, G. Chen, Q. Li, G. Qiu, X. Liu, J. Alloys Compd. 509 (2011) 4104.
[17] R.M. Khafagy, J. Alloys Compd. 509 (2011) 9849.
[18] D.-Y. Wang, A. Leuteritz, B. Kutlu, M. Auf der Landwehr, D. Jehnichen, U. Wagenknecht, G. Heinrich, J. Alloys Compd. 509 (2011) 3497.
[19] T. Wejrzanowski, R. Pielaszek, A. Opalińska, M. Matysiak, W. Lojkowski, K.J. Kurzydlowski, Appl. Surf. Sci. 253 (2006) 204.
[20] R. Pielaszek, Proceedings of the XIX Applied Crystallography Conference, Krakow, Poland, 2003, p. 43.
[21] M.T. Nara, M. Tasumi, J. Phys. Chem. 100 (1996) 19812.
[22] T. Özkaya, M.S. Toprak, A. Baykal, H. Kavas, Y. Köseoğlu, B. Aktaş, J. Alloys Compd. 472 (2009) 18.
[23] S. Wei, Y. Zhu, Y. Zhang, J. Xu, React. Funct. Polym. 66 (2007) 1272.
[24] R. Nyquist, R. Kagel, Infrared Spectra of Inorganic Compounds, Academic Press, New York, 1971.
[25] I.J. Bruce, J. Taylor, M. Todd, M.J. Davies, E. Borioni, C. Sangregorio, T. Sen, J. Magn. Magn. Mater. 284 (2004) 145.
[26] M. Mikhaylova, D.K. Kim, C.C. Berry, A. Zagorodni, M.S. Toprak, A.S.G. Curtis, M. Muhammed, Chem. Mater. 16 (2004) 2344.
[27] B. Ünal, Z. Durmus, H. Kavas, A. Baykal, M.S. Toprak, Mater. Chem. Phys. 123 (2010) 184.
[28] H. Kavas, A. Baykal, M.S. Toprak, Y. Köseoglu, M. Sertkol, B. Aktaş, J. Alloys Compd. 479 (2009) 49.
[29] Z. Durmus, H. Kavas, A. Baykal, H. Sözeri, L. Alpsoy, S.Ü. Çelik, M.S. Toprak, J. Alloys Compd. 509 (2011) 2555.
[30] Z. Durmus, H. Kavas, M.S. Toprak, A. Baykal, T.G. Altınçekiç, A. Aslan, A. Bozkurt, S. Coşgun, J. Alloys Compd. 484 (2009) 371.

[31] B. Ünal, M.S. Toprak, Z. Durmus, H. Sözeri, A. Baykal, J. Nanopart. Res. 12 (2010) 3039.
[32] B. Ünal, Z. Durmus, A. Baykal, H. Sözeri, M.S. Toprak, L. Alpsoy, J. Alloys Compd. 505 (2010) 172.
[33] J. Mürbe, A. Rechtenbach, T. Töpfer, Mater. Chem. Phys. 110 (2008) 426.
[34] B. Aktas, Thin Solid Films 307 (1997) 250–259.
[35] R.H. Kodama, A.E. Berkowitz, E.J. McNiff Jr., S. Foner, Phys. Rev. Lett. 77 (1996) 394.
[36] X. Batlle, A. Labarta, J. Phys. D: Appl. Phys. 35 (2002) R15.
[37] A.E. Berkowitz, J.A. Lahut, I.S. Jacobs, L.M. Levinson, D.W. Forester, Phys. Rev. Lett. 34 (1975) 594.
[38] K. Uzun, E. Cevik, M. Senel, H. Sözeri, A. Baykal, M.F. Abasıyanık, M.S. Toprak, J. Nanopart. Res. 12 (2010) 3057.
[39] N.F. Mott, Philos. Mag. 19 (1969) 835841.
[40] M. Okutan, H.I. Bakan, K. Korkmaz, F. Yakuphanoglu, J. Phys. B: Condens. Matter. 355 (2005) 176.
[41] Z. Richard, The Physics of Amorphous Solids, Wiley–Interscience, New York, 1998.
[42] D. Jana, J. Fort, Physica B 344 (2004) 62.
[43] C. Brosseau, P. Talbot, J. Appl. Phys. 97 (10) (2005) 104325.
[44] H. Kavas, Z. Durmus, A. Baykal, A. Aslan, A. Bozkurt, M.S. Toprak, J. Non-Cryst. Solids 356 (2010) 484.
[45] G.M. Tsangaris, O.C. Psarras, N. Kouloumbi, J. Mater. Sci. 33 (1998) 2027.
[46] S. Abdul-lawad, A. Alnajjar, M.H. Abdallah, Appl. Phys. A: Mater. Sci. Process. 64 (1997) 199.
[47] S. Yu, P. Hing, X. Hu, J. Appl. Phys. 88 (2000) 398.
[48] V. Bobnar, A. Levstik, C. Huang, Q.M. Zhang, J. Non-Cryst. Solids 353 (2007) 205.
[49] K.P. Dillip, R.N.P. Choudhary, B.K. Samantaray, Int. J. Electrochem. Sci. 3 (2008) 597.
[50] Z. Durmus, H. Erdemi, A. Aslan, M.S. Toprak, H. Sözeri, A. Baykal, Polyhedron 30 (2011) 419.